

A Domain-Reduction Approach to Bridging-Scale Simulation of One-Dimensional Nanostructures

Dong Qian^{*1}, Manas Phadke⁺¹, Eduard Karpov² and Wing Kam Liu³

¹School of Dynamic Systems
University of Cincinnati, Cincinnati, OH 45221-0072

²Department of Civil and Materials Engineering
University of Illinois- Chicago, Chicago, 60607-7023

³Department of Mechanical Engineering
Northwestern University, Evanston, IL 60208-0311

Abstract

We present a domain-reduction approach for the simulation of one-dimensional nanocrystalline structures. In this approach, the domain of interest is partitioned into coarse and fine scale regions and the coupling between the two is implemented through a bridging-scale interfacial boundary condition. The atomistic simulation is used in the fine scale region, while the discrete Fourier transform is applied to the coarse scale region to yield a compact Green's function formulation that represents the effects of the coarse scale domain upon the fine/coarse scale interface. This approach facilitates the simulations for the fine scale, without the requirement to simulate the entire coarse scale domain. After the illustration in a simple 1D problem and comparison with analytical solutions, the proposed method is then implemented for carbon nanotube structures. The robustness of the proposed multiscale method is demonstrated after comparison and verification of our results with benchmark results from fully atomistic simulations.

KEY WORDS: nanocrystalline, bridging-scale method, carbon nanotubes, multiscale simulation, Green's function

* Contact author, E-mail: dong.qian@uc.edu, Phone: 1-513-556-0422, Fax: 1-513-556-3390

+ Currently at Cummings, Inc.

1. Introduction

Recent developments in synthesis of one-dimensional nanostructures such as nanowires and nanotubes have provided an exciting new venue for developing light weight, high strength structural components. The unique mechanical and physical properties of these types of nanostructured materials are intimately linked to the structure-property relation that spans across multiple length scales. Correspondingly, multiscale computational method that integrates representations at multiple scales is emerging as a powerful tool in the design and application.

Many of the multiscale methods developed have been based on coupling atomistic simulation method with continuum simulation techniques such as the Finite Element Methods (FEM). As a result, there is a numerical interface between the different simulation methods. Properly treating the continuum/atomistic interface is critical in the implementation of the coupling. At the early stage of the method development, the interface coupling is based on an explicit and direct “handshake” approach. Although not necessary, the FEM mesh is usually refined to the atomic resolution. The FEM nodes typically coincide with the positions of the atoms in the handshake region. The robustness of the method has been extensively demonstrated in quasi-static simulations [1-9]. For finite temperature problem, however, this treatment may lead to artificial phonon reflections due to the differences in the atomistic and continuum representations. Based on the earlier development by Adelman [10-11], a class of interface treatment approach using the Langevin approach have been presented in [12-13]. These approaches are further extended in the bridging-scale method (BSM) [14-29], which was first developed by Wagner and Liu [14] to couple atomistic and continuum scales. An important feature of the method is the decomposition of the field variables through the bridging-scale decomposition. The bridging-domain method is proposed by Xiao and Belytschko [30], in which

the atomic and continuum degrees of freedom are related with the use of Lagrangian multipliers. The conservation properties of the bridge-domain method is further studied in Xu and Belytschko [31]. Li et al [32] proposed the perfect matched layer method in which the phonon reflection is minimized by matching the impedance at the interface. More recently, Chirputkar and Qian [33] developed a space-time version of the BSM approach. This approach is featured by a space-time enrichment based on the extended finite element method. It is shown that this method not only leads to a reflectionless boundary condition at the continuum/atomistic interface but also results in accurate representations of momentum and energy in the simulation of the lattice dynamics. An overview on the development of multiscale models for complex material systems with a special emphasis on the link from quantum-mechanical model [34] to multiscale statistical continuum model is presented in [35] showing the unique advantage of the bridging-scale concept, which enables effective separation of the physical variables that are defined at their relative spatial and temporal scales.

Most of the methodologies proposed above are developed in the context of concurrent simulation, i.e. the continuum simulation is carried out simultaneously with the atomistic simulation. For nanocrystallines, lattice Green's function can be derived to relate the load to the response in the regions modeled as continuum. Therefore, one may substitute the continuum simulation with the use of a lattice Green's function while keeping the atomistic simulation in the fine scale region. The resulting approach is semi-analytical in nature and is referred to as a *domain-reduction approach* in this paper.

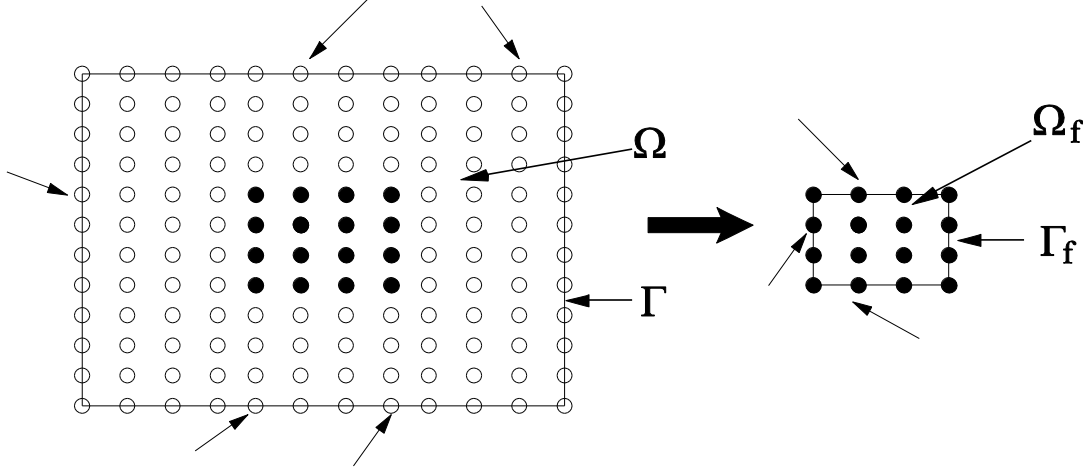


Figure 1. An illustration of the domain-reduction approach.

We first illustrate the domain-reduction idea via Figure 1. We consider the domain Ω occupied by the crystalline system as of which the displacement and traction boundary conditions are defined as Γ_u and Γ_t , respectively and $\Gamma = \Gamma_u \cup \Gamma_t$ and $\Gamma_u \cap \Gamma_t = \emptyset$. The governing equation of the original atomistic system is expressed in terms of the Lagrangian equation [36]

$$\frac{d}{dt} \frac{\partial L}{\partial \dot{\mathbf{r}}_i} - \frac{\partial L}{\partial \mathbf{r}_i} = 0, \quad \forall \mathbf{r}_i \in \Omega \quad (1)$$

in which, $\mathbf{r}_i = (x_i, y_i, z_i)$ is the position vector of atom i . The system's Lagrangian is defined as:

$$L = \sum_{i=1}^N \frac{m_i \dot{\mathbf{r}}_i^2}{2} - U(\mathbf{r}_1, \mathbf{r}_2, \dots, \mathbf{r}_N) \quad (2)$$

The two terms on the right-hand side give the system's kinetic and potential energy, respectively.

Combining Eqs.(1) and (2) yields the equations of motion in the Newtonian form,

$$m_i \ddot{\mathbf{r}}_i = - \frac{\partial U(\mathbf{r}_1, \mathbf{r}_2, \dots, \mathbf{r}_N)}{\partial \mathbf{r}_i} \equiv \mathbf{F}_i^{ext} - \mathbf{F}_i^{int}, \quad \forall \mathbf{r}_i \in \Omega \quad (3)$$

with the initial conditions and external force given by:

$$\mathbf{r}_i = \mathbf{r}_i^0 \text{ and } \dot{\mathbf{r}}_i = \dot{\mathbf{r}}_i^0, \quad \forall \mathbf{r}_i \in \Gamma_u \quad (4)$$

$$\mathbf{F}_i^{ext} = \bar{\mathbf{F}}_i^{ext}, \quad \forall \mathbf{r}_i \in \Gamma_t \quad (5)$$

In many cases, the physics of interest that is related to the problem is localized in a small domain of interest Ω_f rather than in the whole domain Ω . We term Ω_f the fine scale domain and define the coarse scale domain Ω_c through $\Omega = \Omega_c \cup \Omega_f$. Examples of localized physics include strain localization, fracture, dislocation emission from a defect and many others. The corresponding atoms in the fine scale domain are shown as filled dots in Figure 1. From the computational point of view, detailed atomistic representation in Ω_f is important, however, it is impractical to simulate the whole domain Ω with the use of atomistic simulation techniques. On the other hand, the displacement field away from the domain of interest is typically smooth and slow varying, which indicates that the lattice in these regions can be approximated by employing linear assumption. Combining these observations, we now reformulate the original boundary value problem described by Eqs.(3)-(5) as

$$m_i \ddot{\mathbf{r}}_i = - \frac{\partial U(\mathbf{r}_1, \mathbf{r}_2, \dots, \mathbf{r}_N)}{\partial \mathbf{r}_i} \equiv \mathbf{F}_i^{ext} - \mathbf{F}_i^{int}, \quad \forall \mathbf{r}_i \in \Omega_f \quad (6)$$

$$\mathbf{r}_i = \mathbf{r}_i^0, \quad \dot{\mathbf{r}}_i = \dot{\mathbf{r}}_i^0, \quad \forall \mathbf{r}_i \in \Gamma_u^f \quad (7)$$

$$\mathbf{F}_i^{ext} = \bar{\mathbf{F}}_i^{ext}, \quad \forall \mathbf{r}_i \in \Gamma_t^f \quad (8)$$

in which $\Gamma_u^f \cup \Gamma_t^f = \Gamma_f$ is the boundary of the fine scale domain. The goal is then to determine the set of boundary conditions defined on Γ_f such that application of the displacement and traction through Eqs.(7)-(8) would lead to the same solution for the atomic degree of freedom as in the original boundary value problem statement in Eqs.(3)-(5). This implementation results in a

reduction to an equivalent problem defined on a relatively smaller fine scale domain as compared with the original problem.

It is instructive to look at the domain-reduction approach from the perspective of decomposition of the displacement field. We define the sum of the displacement \mathbf{u} through

$$\mathbf{u} = \bar{\mathbf{u}} + \mathbf{u}' \tag{9}$$

in which $\bar{\mathbf{u}}$ is the coarse scale displacement and \mathbf{u}' is the fine scale displacement. The terms coarse and fine are defined in a relative sense and depends on the choices of Ω_f and Ω_c . In our approach we let $\mathbf{u} = \bar{\mathbf{u}}$ on Ω_c and $\mathbf{u} = \mathbf{u}'$ on Ω_f . This in turn implies that $\mathbf{u}' = 0$ on Ω_c and $\bar{\mathbf{u}} = 0$ on Ω_f according to the decomposition from Eq. (9). Our strategy is to treat $\bar{\mathbf{u}}$ analytically and then solve \mathbf{u}' through numerical approach by taking into account of the effect from $\bar{\mathbf{u}}$ based on a Green's function approach. As shown in the rest of the paper, two types of lattice Green's functions are incorporated in the boundary condition Γ_f , one due to the far-field effect and the other from the interaction at the coarse/fine scale interface, which is defined as the near-field effect. Here we make use of the Green's functions that allow us to fully consider both the far- and near-field effects.

The rest of the paper is organized as follows: Section 2 outlines the formulation of the proposed domain-reduction approach based on the use of bridging-scale interfacial boundary condition. To enable better understanding of the method, we provide a simple introduction on the fundamentals of the Discrete Fourier Transform. We then demonstrate its use for arriving at the bridging-scale boundary condition expressed in terms of the lattice Green's function. We proceed in section 3 to verify the formulation for a simple 1D problem. The simplicity of the problem allows us to provide an analytical proof of the developed formulation. In section 4, we

make extensions to the study of carbon nanotubes as an example of one-dimensional nanocrystalline. In this system, the inter-atomic interaction is governed by the combination of pair and three-body potentials. Extensive examples are provided in section 5 to show the robustness of the method. Final conclusions are made in section 6.

2. The Proposed Methodology

The proposed method makes extensive use of the Discrete Fourier Transform (DFT) technique, which is a mathematical formulation to transform spatially varying functions from real space to a wave-number space and is, by definition, performed on infinite periodic structures. For a periodic function f of a discrete (integer) spatial parameter l , the most general form of DFT is given by

$$F_{l \rightarrow k}[f(l)] = \hat{f}(k) = \sum_l f(l)e^{-ikl} \quad (10)$$

where $\hat{f}(k)$ is the image in the wave number space of the spatial function $f(l)$, l is an integer and k is a real number and i is the imaginary number $\sqrt{-1}$.

Conversely, the inverse Discrete Fourier Transform of a function in the wave number space is given by:

$$F^{-1}[\hat{f}(k)] = f(l) = \frac{1}{2\pi} \sum_k \hat{f}(k)e^{ikl} \quad (11)$$

The Fourier domain function $\hat{f}(k)$ is a 2π -periodic function of wave number k . The choice of the wave number k is not unique and depends on the periodicity of the function $f(l)$.

For example, for an $N+1$ periodic function, k takes the form

$$k = \frac{2\pi p}{N+1}, \quad p = 0, 1, 2, \dots, N \quad (12)$$

Then the Fourier Transform and the inverse Fourier Transform are given by

$$F_{l \rightarrow p}[f(l)] = \hat{f}(p) = \sum_{l=0}^N f(l) e^{\frac{-i2\pi pl}{N+1}} \quad (13)$$

$$F^{-1}[f(k)] = f(l) = \frac{1}{N+1} \sum_{p=0}^N f(k) e^{\frac{i2\pi pl}{N+1}} \quad (14)$$

If f and g are two periodic functions in the real space, then their convolution summation $f * g$ is defined as

$$(f * g)(l) = \sum_{l'} f(l') g(l - l') \quad (15)$$

The convolution theorem then states that the Fourier transform of the convolution summation of two functions in real space is equal to the product of the transforms of individual functions in the wave number space. For the periodic functions f and g in the real space, the convolution theorem yields:

$$F_{l \rightarrow p}[(f * g)(l)] = \hat{f}(p) \hat{g}(p) \quad (16)$$

Application of DFT to static analysis has been made by Ryvkin et al [37] for optimal design of infinite repetitive beam like structures, while a general methodology for static analysis of periodic structures is due to Moses [38]. An elaborate discussion on functional solutions for spatially repetitive structures using DFT can be found in [39-40].

2.1 Coarse-scale Analysis

2.1.1 Exploiting the Crystalline Periodicity

For the purpose of simplicity, we consider a 1D periodic nanostructure that is generated by translating a unit cell along a single axis (Figure 2a). It can be realized that the global

stiffness matrix of such a repetitive mechanical structure shall have non-zero stiffness values K_{ij} only in those locations where the indices i and j represent the degrees of freedom of the same node or of nodes that share structural elements between them. Moreover, if the deformation is homogeneous, the structural stiffness shall inherit the periodicity property from the crystal structure. As such, the global stiffness matrix shall consist of only a repeating set of smaller sub-matrices corresponding to any unit cell, which are placed in rows symmetrically with respect to the diagonal of the global stiffness matrix (Figure 2b).

It is important to note that there are two possible scenarios in which the periodicity assumption holds. The first is based on the small deformation assumption in which the stiffness values in the undeformed configuration are used. The corresponding formulation will be referred to as a total formulation since the total values of the displacement terms are being directly dealt with. In the second case, the structure undergoes large homogeneous deformation. In this case, we have chosen to treat the periodicity of the structural tangent stiffness rather than the stiffness itself. This results in an incremental formulation. In this section and section 3, we outline our theory and the 1D illustration based on the total formulation for the purpose of simplicity. The extension to the incremental formulation and application to the CNT structure will be discussed in section 4.

With the periodicity assumption, it is possible to obtain the three sub-matrices K_1 , K_0 , and K_{-1} corresponding to any unit cell such that K_0 relates the stiffness of the elements within the unit cell, while K_1 and K_{-1} represent respectively the right and left hand coupling between the adjacent cell locations. A part of the global stiffness matrix of such a geometrically repeating structure consisting of N unit cells in the coarse scale region is shown in Figure 2b. The N displacement and force vectors correspond to the N unit cells in the coarse scale region of the

2.1.2 Implementing the Discrete Fourier Transform

For any arbitrary unit cell in the periodic coarse scale region, Eq.(17) can be rewritten in the discrete convolution form as:

$$\sum_{l'=l-1}^{l+1} K_{l-l'} u_{l'} = -f_l \quad (18)$$

in which we have defined $f_l = -f_l^{\text{int}}$. Taking the Discrete Fourier Transform (DFT) of both sides leads to

$$\sum_{l=0}^N \sum_{l'=l-1}^{l+1} K_{l-l'} u_{l'} e^{-i2\pi p \frac{l}{N+1}} = -\sum_{l=0}^N f_l e^{-i2\pi p \frac{l}{N+1}} \quad (19)$$

Now, we multiply and divide the left-hand side of the Eq.(14) by $e^{-i2\pi p \frac{l'}{N+1}}$, to obtain

$$\sum_{l=0}^N \sum_{l'=l-1}^{l+1} K_{l-l'} e^{-i2\pi p \frac{(l-l')}{N+1}} u_{l'} e^{-i2\pi p \frac{l'}{N+1}} = -\sum_{l=0}^N f_l e^{-i2\pi p \frac{l}{N+1}} \quad (20)$$

Next we introduce the parameter $s = l - l'$ and rearrange to give

$$\sum_{s=-1}^1 K_s e^{-i2\pi p \frac{s}{N+1}} \sum_{l=0}^N u_{(l-s)} e^{-i2\pi p \frac{(l-s)}{N+1}} = -\sum_{l=0}^N f_l e^{-i2\pi p \frac{l}{N+1}} \quad (21)$$

Due to $(N+1)$ periodicity of the lattice, we have

$$\sum_{l=0}^N u_{(l-s)} e^{-i2\pi p \frac{(l-s)}{N+1}} = \sum_{l=0}^N u_l e^{-i2\pi p \frac{l}{N+1}} \quad (22)$$

The transformed governing equation thus takes the form,

$$\widehat{K}(p) \widehat{u}(p) = -\widehat{f}(p), \text{ for } p = 0, 1, 2, 3 \dots N \quad (23)$$

where, the Fourier images of functions K , u and f assumed $N+1$ periodic, are given as:

$$\widehat{K}(p) = \sum_{s=-1}^1 K_s e^{-i2\pi p \frac{s}{N+1}} \quad (24)$$

$$\widehat{u}(p) = \sum_{l=0}^N u_l e^{-i2\pi p \frac{l}{N+1}} \quad (25)$$

$$\widehat{f}_l(p) = \sum_{l=0}^N f_l e^{-i2\pi p \frac{l}{N+1}} \quad (26)$$

The respective Fourier images of the functions retain their sizes in the wave number space. Alternatively, the application of convolution theorem yields the same result in Eq.(23).

2.2 Boundary Conditions

In accordance with the definition of Discrete Fourier Transform, we formally treat the coarse scale domain as a part of a larger domain with periodic boundary conditions, whose deformation occurs only due to some external forces on the boundary cells $l = 0$ and $l = N$. The traction boundary condition is defined by the equation:

$$f_l^{ext} = \delta_{l,0} f_0 + \delta_{l,N} f_N \quad (27)$$

in which f_0 and f_N are respectively the vectors of external forces on the virtual boundary cell $l=0$ and the actual boundary cell $l=N$ and δ is Kronecker delta.

Hence Eq.(27) can be written as:

$$\widehat{f}(p) = f_0 + f_N e^{-i2\pi p \frac{N}{N+1}} \quad (28)$$

Now pre-multiplying Eq.(23) by the inverse of the Fourier domain representation of the kernel function matrix gives us:

$$\widehat{u}(p) = -\widehat{K}(p)^{-1} \widehat{f}(p) \quad (29)$$

The advantage of using DFT for periodical structures can be shown by comparing Eq.(29) with the one in Figure 2 and observing that instead of solving the inverse of the global stiffness matrix of the size of $NDOF \times NDOF$, where $NDOF$ is the total number of degrees of

freedom of the entire structure, we need only to handle the inverse of \hat{K} with size $na \times na$, na being the number of degrees of freedom of any l^{th} unit cell.

Now, applying inverse DFT to Eq.(29) we obtain displacement u_l as:

$$u_l = \frac{1}{N+1} \sum_{p=0}^N \hat{u}(p) e^{i2\pi p \frac{l}{N+1}} = \frac{1}{N+1} \sum_{p=0}^N -\hat{K}(p)^{-1} \hat{f}(p) e^{i2\pi p \frac{l}{N+1}} \quad (30)$$

Further, we substitute the Fourier image $\hat{f}(p)$ from Eq.(26) into (30) with index l changed to l' for clarity. Thus,

$$u_l = \frac{1}{N+1} \sum_{p=0}^N -\hat{K}(p)^{-1} \sum_{l'=0}^N f_{l'} e^{-i2\pi p \frac{l'}{N+1}} e^{i2\pi p \frac{l}{N+1}} = \sum_{l'=0}^N G_{ll'} f_{l'} \quad (31)$$

where the function $G_{ll'}$, which is essentially the Green's function, is given as:

$$G_{ll'} = \frac{1}{N+1} \sum_{p=0}^N -\hat{K}(p)^{-1} e^{i2\pi p \frac{l-l'}{N+1}} \quad (32)$$

The force term $f_{l'}$ in Eq.(31) is defined completely by vectors f_0 and f_N as shown in Eq.(27). Since $f_{l'}$ is completely independent of the parameters l and p , it contributes merely as a constant multiplying factor to the Green's function in the transform process.

2.3 The Green's Function

The Green's function in Eq.(32) essentially represents the inverse DFT of the quantity $-\hat{K}(p)^{-1} e^{-i2\pi p \frac{l'}{N+1}}$ and can be expressed as

$$G_{ll'} = F_{p \rightarrow l}^{-1} \left(-\hat{K}(p)^{-1} e^{-i2\pi p \frac{l'}{N+1}} \right) \quad (33)$$

In numerical implementation of the inverse transform, we make use of half integer wave numbers such that p takes the values $p = \pm 1/2, \pm 3/2, \dots, \pm N \mp 1/2$. The Green's function is then defined as

$$G_{ll'} = -\frac{1}{2N} \sum_{p=1/2-N}^{N-1/2} \hat{K}(p)^{-1} e^{\frac{i2\pi p(l-l')}{2N}} \quad (34)$$

The matrix function $G_{ll'}$ can be computed for all the nodes in the coarse scale domain. Up to a rigid body motion, the r^{th} column of the Green's function matrix represents the deflections of the l^{th} nodal set caused by the r^{th} component of a unit load vector applied to the l^{th} nodal location of the repetitive framework. The displacement solution of any l^{th} ring of atoms can then be described in terms of Green's function $G_{ll'}$ which is a function of parameters l and l' .

Substituting Eq.(27) into Eq.(31), the latter can now be expressed in terms of the Green's functions as

$$u_l = G_{l0}f_0 + G_{lN}f_N \quad (35)$$

2.4 Convolution Operators Θ and Ξ

We expand Eq.(35) at locations $l=0$ and $l=N$ as:

$$u_0 = G_{00}f_0 + G_{0N}f_N \quad (36)$$

$$u_N = G_{N0}f_0 + G_{NN}f_N \quad (37)$$

Solving for the inverses in the matrix form gives:

$$\begin{Bmatrix} f_0 \\ f_N \end{Bmatrix} = \begin{bmatrix} G_{00} & G_{0N} \\ G_{N0} & G_{NN} \end{bmatrix}^{-1} \begin{Bmatrix} u_0 \\ u_N \end{Bmatrix} = G^{-1} \begin{Bmatrix} u_0 \\ u_N \end{Bmatrix} \quad (38)$$

Next we define

$$H = \begin{bmatrix} H_{00} & H_{0N} \\ H_{N0} & H_{NN} \end{bmatrix} = G^{-1} = \begin{bmatrix} G_{00} & G_{0N} \\ G_{N0} & G_{NN} \end{bmatrix}^{-1} \quad (39)$$

Hence we have

$$f_0 = H_{00}u_0 + H_{0N}u_N \quad (40)$$

$$f_N = H_{N0}u_0 + H_{NN}u_N \quad (41)$$

The displacement for $l=1$ can be written according to Eq.(30) as:

$$u_1 = G_{10}f_0 + G_{1N}f_N \quad (42)$$

Substituting Eq.(40) and (41) into Eq.(42) gives:

$$u_1 = (G_{10}H_{00} + G_{1N}H_{N0})u_0 + (G_{10}H_{0N} + G_{1N}H_{NN})u_N \quad (43)$$

or equivalently

$$u_1 = \Theta u_0 + \Xi u_N \quad (44)$$

where $\Theta = (G_{10}H_{00} + G_{1N}H_{N0})$ and $\Xi = (G_{10}H_{0N} + G_{1N}H_{NN})$

Thus the sought operators of bridging-scale boundary conditions for periodic lattices are square matrices which can be given by the matrix multiplication:

$$\begin{pmatrix} \Theta & \Xi \end{pmatrix} = \begin{pmatrix} G_{10} & G_{1N} \end{pmatrix} \begin{pmatrix} H_{00} & H_{0N} \\ H_{N0} & H_{NN} \end{pmatrix} \quad (45)$$

Eq.(44) expresses the displacement vector u_1 in terms of the vectors u_0 and u_N . Thus, with the availability of vectors u_0 and u_N and the mathematical operators as obtained in Eq.(45), it is possible to obtain the displacement vector u_1 without analyzing the entire coarse scale domain of the repetitive structure.

In general, an analytical expression for Eq.(43) is not possible due to the presence of DFT and inverse DFT in the same equation. Here, we take the advantage of the translational symmetry in the axial direction of the periodic lattice so that we have

$$K_1 = K, \quad K_0 = -(K + K^T) + \tilde{K}, \quad K_{-1} = K^T \quad (46)$$

in which K represents the interactions among atoms between the cells and \tilde{K} represents the interaction of atoms within the cells. Hence the DFT operation can be performed analytically to get:

$$\hat{K}(k) = (K + K^T)(\cos(k) - 1) + \tilde{K} + i(K - K^T)\sin(k) \quad (47)$$

in which $k = \frac{\pi p}{N}$.

Alternatively, this can be written as:

$$\hat{K}(k) = A(k)(I + iB(k)) \quad (48)$$

in which I is the identity matrix of the same order as K , with

$$A = (K + K^T)(\cos k - 1) + \tilde{K}, \text{ and } B = A^{-1}(K - K^T)\sin k \quad (49)$$

The inverse of $\hat{K}(k)$ is then given as

$$\hat{K}(k)^{-1} = (I + B^2(k))^{-1} (I - iB(k)) A^{-1}(k) \quad (50)$$

2.5 Fine Scale Analysis

With the bridging-scale boundary condition derived in the previous sections, it is now possible to focus on the fine scale region with the displacement u_1 applied to the periphery of the fine scale region. It is applied such that it produces the same effect in the fine scale region as u_N applied to the periphery of the coarse scale region. With this equivalent boundary condition, the classical atomistic simulation method can be performed just over the fine scale region. In this paper, we focus on the molecular mechanics approach and neglect the dynamic effect. For the carbon nanotube system considered, we use the Brenner's potential [41] to model the potential energy of the system as a function of atomic interactions. Detailed implementation will be discussed in sections 4 and 5.

3. One Dimensional Nanostructure Analysis

Before application to 3D structures, we verify the validity of the formulation using a one-dimensional periodic mono-atomic chain with each atom having a single longitudinal degree of freedom.

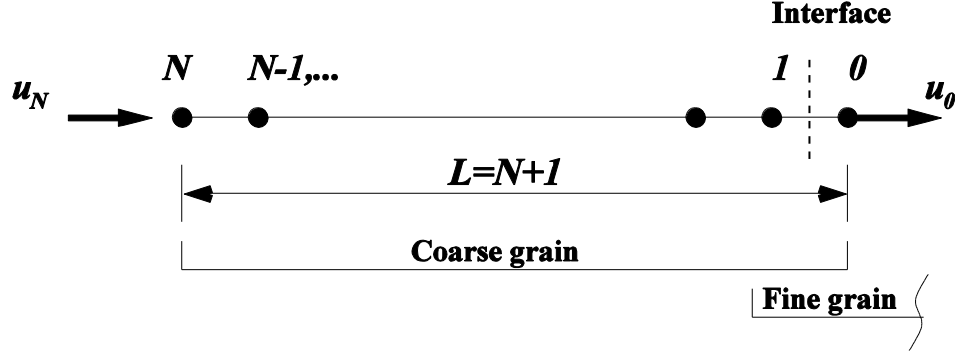


Figure 3. One dimensional mono-atomic chain assumed $(N+1)$ periodic.

As shown in Figure 3, atom N represents the peripheral boundary of the coarse scale region and atoms 1 and 0 represent the interface between the coarse and fine scale regions. Taking into account the uniform equilibrium deformation character of this periodic lattice, we can obtain the displacement of atom 1 (u_1) in terms of displacements of atom 0 (u_0) and atom N (u_N) by evaluating at atom 1, a first order interpolation polynomial satisfying displacements at nodes 0 and N as:

$$u_1 = \frac{N-1}{N}u_0 + \frac{1}{N}u_N \quad (51)$$

Thus in verifying our formulation, we seek to obtain the same expression for displacement u_1 as given by Eq.(51).

For the one dimensional case at hand, Eq.(13) can be expanded at the location $l = 0$ to give:

$$K_{-1}u_1 + K_0u_0 + K_1u_{-1} = f_0^{\text{int}} \quad (52)$$

The quantity u_{-1} in Eq.(52) represents the displacement of that neighbor of atom 0 that lies completely in the fine scale region.

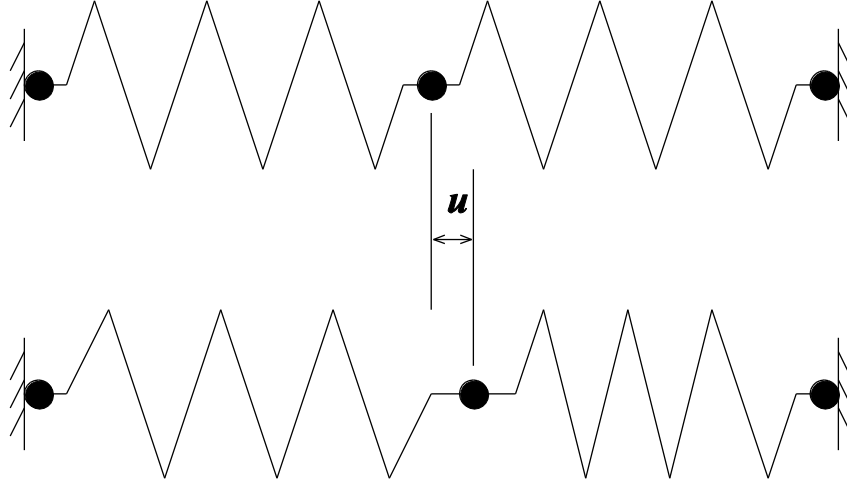


Figure 4. Covalent bonds between carbon atoms analogous to springs of linear stiffness constants K .

Figure 4 shows a unit cell consisting of a single carbon atom bonded to two other identical atoms. Atoms are shown as shaded circles while the chemical bonds are represented by springs with identical linear constants K . It also represents the left and right stiffness couplings of the l^{th} unit cell. The kernel functions K_1 , K_0 and K_{-1} are obtained by measuring the interaction forces while displacing the atom. For the one dimensional case being considered here, these reduce to scalar quantities in terms of a linear interaction coefficient K such that:

$$K_{\pm 1} = K, \quad K_0 = -2K \quad (53)$$

According to Eq.(44) and Eq.(45), $A = 2K(\cos(k) - 1)$ and $B = 0$,

$$\hat{K}(k)^{-1} = \frac{1}{2K(\cos(k) - 1)} \quad (54)$$

Hence, using Eq.(29) and Eq.(54), the lattice Green's function for the one dimensional case is given as:

$$G_{ll'} = -\frac{1}{2K} \frac{1}{2N} \sum_{p=1/2-N}^{N-1/2} \frac{e^{\frac{i\pi p(l-l')}{N}}}{\cos(\pi p/N) - 1} \quad (55)$$

Using Euler's formula ($e^{i\theta} = \cos\theta + i\sin\theta$), $\cos(-\theta) = \cos(\theta)$ and $\sin(-\theta) = -\sin(\theta)$, we observe that the imaginary part of Eq.(55) reduces to zero due to symmetry of the summation about $p=0$. We can then rewrite Eq.(55) as

$$G_{ll'} = -\frac{1}{2K} \frac{2}{2N} \sum_{p=1/2}^{N-1/2} \frac{\cos(\pi p(l-l')/N)}{\cos(\pi p/N) - 1} \quad (56)$$

Using the half angle identity $\cos\theta = 1 - 2\sin^2(\theta/2)$ in the denominator of Eq.(56), we get:

$$G_{ll'} = -\frac{1}{2K} \frac{1}{N} \sum_{p=1/2}^{N-1/2} \frac{\cos(\pi p(l-l')/N)}{-2\sin^2(\pi p/2N)} \quad (57)$$

Changing the bounds of the summation, we can express Eq.(57) as:

$$G_{ll'} = \frac{1}{2K} \frac{1}{2N} \sum_{p=1}^N \frac{\cos(\pi(2p-1)(l-l')/2N)}{\sin^2(\pi(2p-1)/4N)} \quad (58)$$

Substituting $2N = n$ in Eq.(58), we have

$$G_{ll'} = \frac{1}{2K} \frac{1}{2N} \sum_{p=1}^{n/2} \frac{\cos(\pi(2p-1)(l-l')/n)}{\sin^2(\pi(2p-1)(l-l')/2n)} \quad (59)$$

Based on [42-43] and Appendix A, we have

$$\sum_{p=0}^{(n-2)/2} \frac{\cos(\pi(2p+1)m/n)}{\sin^2(\pi(2p+1)/2n)} = \frac{n}{2}(n-2m) + \frac{1}{4} [(-1)^n - 1] (-1)^m \text{ for } m = 0, 1, 2, \dots, n \quad (60)$$

Changing the bounds of the summation again, we can express Eq.(60) as

$$\sum_{p=1}^{n/2} \frac{\cos(\pi(2p-1)m/n)}{\sin^2(\pi(2p-1)/2n)} = \frac{n}{2}(n-2m) + \frac{1}{4} [(-1)^n - 1] (-1)^m \quad (61)$$

Substituting Eq.(61) into Eq.(59) where $m = (l-l')$ we get

$$G_{ll'} = \frac{1}{2K} \frac{1}{2N} \left(\frac{n}{2} (n - 2(l - l')) + \frac{1}{4} [(-1)^n - 1] (-1)^m \right) \quad (62)$$

Substituting back $n = 2N$ we have

$$G_{ll'} = \frac{1}{2K} \frac{1}{2N} \left(N(2N - 2(l - l')) + \frac{1}{4} [(-1)^{2N} - 1] (-1)^m \right) \quad (63)$$

$$G_{ll'} = \frac{1}{2K} (N - (l - l')) \quad (64)$$

Although the proof of Eq.(64) is stated only for non-negative values of m , it can be extended for negative values of m , more specifically for the term G_{lN} in Eq.(42). Employing numerical methods for terms with $l' > l$, we observe that $G_{ll'}$ takes the form $G_{ll'} = \frac{1}{2K} (N - (l' - l))$.

Thus the most general form of the Green's function can be stated as:

$$G_{ll'} = \frac{1}{2K} (N - |l - l'|) \quad (65)$$

Substituting $G_{ll'}$ in Eq.(34) we obtain:

$$H = \begin{bmatrix} H_{00} & H_{0N} \\ H_{N0} & H_{NN} \end{bmatrix} = G^{-1} = \begin{bmatrix} G_{00} & G_{0N} \\ G_{N0} & G_{NN} \end{bmatrix}^{-1} = \frac{1}{2K} \begin{bmatrix} N & N - N \\ N - N & N \end{bmatrix}^{-1} = \frac{2K}{N^2} \begin{bmatrix} N & 0 \\ 0 & N \end{bmatrix} \quad (66)$$

Substituting values from Eq.(66) in Eq.(44), we have,

$$\Theta = \frac{(N-1)(N)}{N^2} = \frac{N^2 - N}{N^2} = \frac{N(N-1)}{N^2} = \frac{(N-1)}{N}$$

$$\Xi = \frac{(N - \text{abs}(1 - N))(N)}{N^2} \quad (67)$$

For $N > 1$,

$$\Xi = \frac{(N - (N-1))(N)}{N^2} = \frac{N}{N^2} = \frac{1}{N} \quad (68)$$

The Green's function operators for the one dimensional case are thus given by:

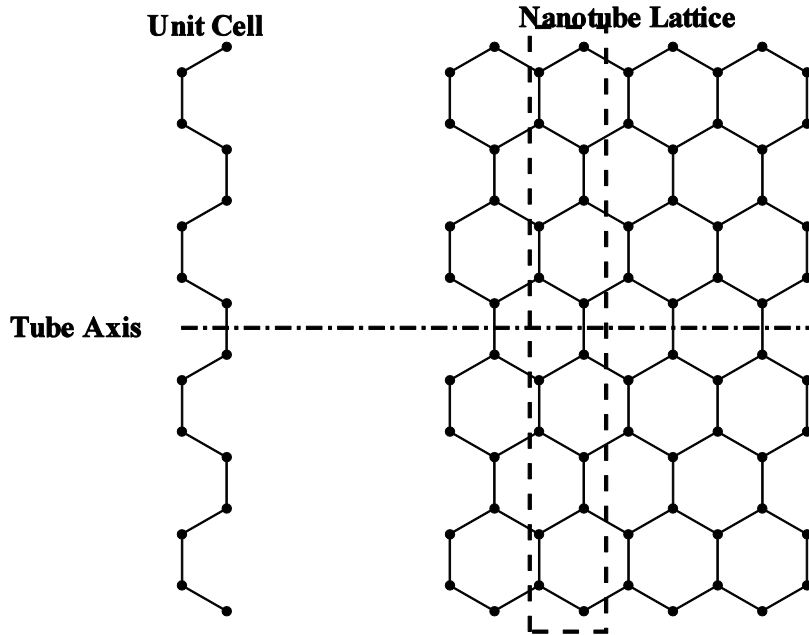
$$\Theta = \frac{N-1}{N}, \quad \Xi = \frac{1}{N} \quad (69)$$

It can now be observed that implementation of the proposed coarse scale analysis to one-dimensional problems yields field solutions exactly the same as the analytical results as shown in Eq.(51).

4. Extension to Carbon Nanotubes

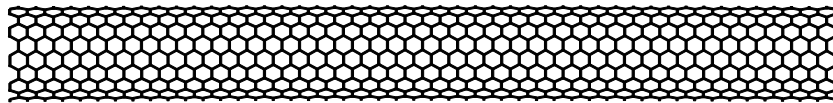
4.1 Periodic Geometry of Carbon Nanotubes

As a cylindrical shaped molecule, the orientation of the carbon bonds with respect to the nanotube axis determines the chirality of the nanotube [44]. It is important to recognize that nanotubes of any chirality can be considered to be a pattern or arrangement of bonded carbon atoms that repeats itself periodically in the axial direction of a nanotube. We consider the example of a single walled armchaired nanotube. Figure 5(a) shows a unit cell in two dimensions, consisting of a set of carbon atoms, which when translated along the axial direction along with its associate substructure generates a graphene sheet shown in Figure 5(b). The graphene sheet when rolled in the direction perpendicular to the tube axis generates the nanotube as shown in Figure 5(c). Zigzag and chiral nanotubes can similarly be thought of as being generated by axial translation of similar unit cells.



(a) Periodic Unit cell of carbon atoms

(b) Nanotube lattice



(c) The generated nanotube

Figure 5. Periodic geometry of CNTs.

4.2 Multiscale Analysis

We applied the method for the analysis of carbon nanotubes. For the sake of simplicity, we apply symmetric boundary conditions at the two ends of the tube. Thus we have a central fine scale region and two identical coarse scale regions placed symmetrically on either side of the fine scale region. We identify each unit cell in the coarse scale region with a non-negative integer ' l '. While the unit cells at the interfaces between the coarse and the fine scale regions are the 0^{th} unit cells, the terminating unit cell at each end is the N^{th} unit cell. Owing to symmetry of the structure and the applied boundary conditions, it shall suffice to consider only one interface

between the fine and the coarse scale region. Figure 6 shows the idea of introducing a virtual interlayer between the coarse and fine scale regions.

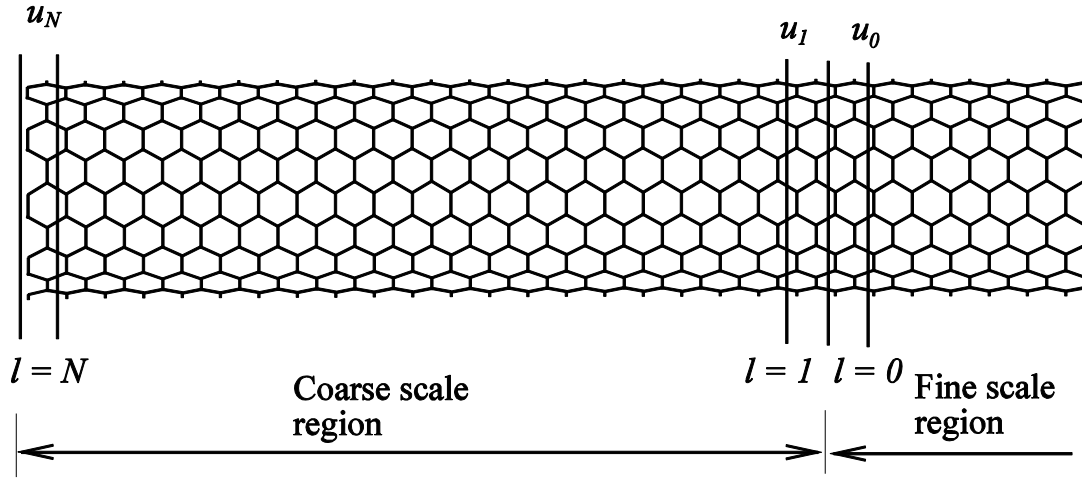


Figure 6. Multiscale discretization scheme for the analysis of carbon nanotubes.

4.3 Fine Scale Analysis

The covalent bonds between the sp^2 hybridized carbon atoms in CNTs undergo stretching, twisting and bending under the application of external forces. Classical molecular mechanics predicts the energy of molecules under loading conditions as a function of their degrees of freedom using empirical inter-atomic potentials. Bonding potentials are useful in modeling the covalent bonds in the CNTs in order to predict their trajectories under constrained conditions.

Based on the study of Abell [45], Brenner put forth a bond order model of an inter-atomic potential that takes in to account the effect of formation and breakage of the C-C bonds. In this paper, the Brenner potential [41] is applied to C-C bonds in the CNTs, given by:

$$E = \sum_i \sum_{j \neq i} [V_R(r_{ij}) - \bar{B}_{ij} V_A(r_{ij})] \quad (70)$$

where r_{ij} is the distance between an atom i and its neighbor j and the attractive term ($V_A(r_{ij})$) and repulsive term ($V_R(r_{ij})$) are given by

$$V_R(r_{ij}) = f_{ij}(r_{ij})D_{ij}^{(e)} / (S_{ij} - 1)e^{-\sqrt{2S_{ij}}\beta_{ij}(r-R_{ij}^{(e)})} \quad (71)$$

$$V_A(r_{ij}) = f_{ij}(r_{ij})D_{ij}^{(e)}S_{ij} / (S_{ij} - 1)e^{-\sqrt{2/S_{ij}}\beta_{ij}(r-R_{ij}^{(e)})} \quad (72)$$

The attractive term accounts for cross-atomic attractive forces between any atomic nucleus and the electron clouds of surrounding atoms while the repulsive term accounts for the mutual repulsive forces between positively charged nuclei in each other's vicinity. The piecewise defined continuous function $f_{ij}(r_{ij})$ restricts the pair potential to the nearest neighbors and is given by:

$$f_{ij}(r) = \begin{cases} 1, & r < R_{ij}^{(1)} \\ \frac{1}{2} + \frac{1}{2} \cdot \cos \left[\frac{\pi(r - R_{ij}^{(1)})}{(R_{ij}^{(2)} - R_{ij}^{(1)})} \right], & R_{ij}^{(1)} \leq r \leq R_{ij}^{(2)} \\ 0, & r > R_{ij}^{(2)}, \end{cases} \quad (73)$$

$R_{ij}^{(1)}$ and $R_{ij}^{(2)}$ are cut-off radii corresponding to bond stretching and breaking respectively. The cut-off function $f_{ij}(r)$ serves the purpose of truncating the computation so as to accommodate only the interactions of atoms with other atoms within a certain cutoff radius. The middle interval trigonometric function in Eq.(73) assures a smooth transition of $f_{ij}(r)$ from 1 to 0 when the value of the inter-atomic distance approaches the cut-off radius $R_{ij}^{(2)}$. The zero value of the cut-off function for $r > R_{ij}^{(2)}$ helps disregard the interactions between atoms separated by a distance more than the cut-off radius.

The empirical bond order function \bar{B}_{ij} represents the multi-body coupling effects that account for the specifics of the local atomistic environment of atom i and is given by:

$$\bar{B}_{ij} = (B_{ij} + B_{ji}) / 2 \quad (74)$$

where

$$B_{ij} = \left(1 + \sum_{k(\neq i, j)} G_i(\theta_{ijk}) \cdot f_{ik}(r_{ik}) \right)^{-\delta_i} \quad (75)$$

Here, r_{ik} is the distance between atoms i and k and θ_{ijk} is the angle between the bonds i - j and i - k , such that k represents all the neighbors of atom i other than j within the cut-off radius.

The function G in Eq.(75) is given by

$$G_i(\theta) = a_0 \{1 + c_0^2 / d_0^2 - c_0^2 / [d_0^2 + (1 + \cos \theta)^2]\} \quad (76)$$

The parameters $D_{ij}^{(e)}$, $R_{ij}^{(e)}$, β and S_{ij} in equations (71) and (72), $R_{ij}^{(1)}$ and $R_{ij}^{(2)}$ in Eq.(73), δ in Eq.(75) and a_0 , c_0 and d_0 in Eq.(76) have been determined by Brenner for systems involving carbon bonds and systems involving carbon and hydrocarbon bonds and can be found in [41].

Equilibrium configurations under application of boundary conditions are obtained by minimizing the energy determined using the Brenner potential. As applied to the multiscale analysis at hand, the boundary conditions for the fine scale region are the displacements of atoms in the unit cell corresponding to $l=1$ in the coarse scale region. The procedure for the analysis of the fine scale region is outlined, in brief, as follows:

1. The atomic coordinates of the nanotube are initially read from an input file. These coordinates do not necessarily represent the equilibrium configuration and are relaxed to reach equilibrium in the first step. Displacement boundary conditions are not applied to the coarse scale region during this first relaxation step.

2. Depending on the dictating boundary conditions d_N , the displacement d_l is determined using Eq.(39) and is applied as the boundary condition to the fine scale region of the CNT.
3. The potential energy of the system, using Brenner's bond order model, and its derivative corresponding to the molecular configuration are calculated.
4. For every incremental displacement imposed, the potential energy is minimized using the limited memory BFGS algorithm [46], with displacements d_l as the bounding constraints. The atomic configuration corresponding to the minimum energy represents the response behavior of the fine scale region to the externally applied displacement d_N .
5. Incremental displacements d_N are applied on the coarse scale region and steps 2 through 5 are repeated till the desired deformation is attained.

4.4 Coarse Scale analysis

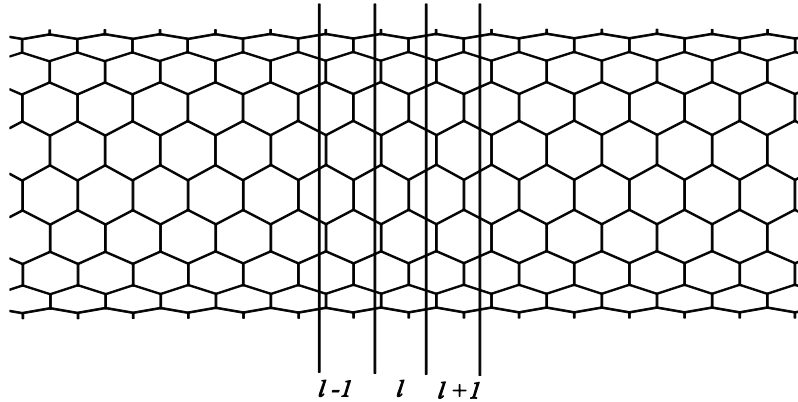


Figure 7. Nanotube unit cell.

For the coarse scale region, we assume moderately deformed carbon nanotubes and bonded interactions are short-ranged and include only up to second nearest neighbors. Hence the forces acting on the atoms of any l^{th} unit cell are affected only by the atoms in the $(l+1)^{th}$ and $(l-1)^{th}$ unit cells. Figure 7 shows the interaction of any unit cell l with its adjacent unit cells on both sides. In

the case of small deformation assumption, the governing equilibrium equation for any unit cell in the coarse scale region can be written as:

$$\sum_{l'=l-1}^{l+1} K_{l-l'} u_{l'} = f_l^{\text{int}} \quad (77)$$

where $K_{l-l'}$ are the kernel sub-matrices, $u_{l'}$ are the vectors of displacements of the atoms of the l' th unit cells, and f_l^{int} is the internal force vector on the l^{th} unit cell. The K matrices in Eq.(77) are invariant for any unit cell and are defined by the structure of internal forces i.e. as a function of the potential energy U utilized in terms of displacements about equilibrium positions:

$$K_{l-l'} = \left. \frac{\partial f_l^{\text{int}}}{\partial u_{l'}} \right|_{u=0} \quad (78)$$

where

$$f_l^{\text{int}} = -\frac{\partial U(u)}{\partial u_l} \quad (79)$$

Application of Discrete Fourier Transform and subsequently its inverse generates two dimensional Green's function matrices defined as:

$$G_{ll'} = F_{p \rightarrow l}^{-1} \{ \hat{G}(p) \} = \frac{1}{2N} \sum_{p=\frac{1}{2}-N}^{\frac{N-1}{2}} \hat{G}(p) e^{\frac{i\pi p(l-l')}{N}} \quad (80)$$

Here,

$$\hat{G}(p) = -\hat{K}^{-1}(p) \equiv -(F \{ K_l \})^{-1} = -(K_{-1} e^{ip} + K_0 + K_1 e^{-ip})^{-1} \quad (81)$$

Knowledge of the stiffness sub-matrices and mathematical manipulation following equations (14) through (40) leads to generation of the sought mathematical operators Θ and Ξ . It can be observed that the mathematical operators are governed solely by the inter-atomic potential and the parameter N .

In most of the examples to be shown below, large deformation is involved and the use of the stiffness based on the original undeformed configuration based on Eq.(78) may not be accurate. As an alternative, we extend it into an incremental formulation and obtain the solution within an incremental loading step. In the incremental formulation, we assume the periodicity of the tangent stiffness rather than the stiffness itself. Corresponding to Eq.(77), the incremental form of the equilibrium equation for the coarse scale domain can be given as

$$\sum_{l'=l-1}^{l+1} K_{l-l'}^{(n)} \Delta u_{l'}^{(n)} = \Delta f_l^{\text{int}(n)} \quad (82)$$

in which $\Delta u_{l'}^{(n)}$, $\Delta f_l^{\text{int}(n)}$ are the incremental displacement and force vectors corresponding to the l -th unit cell for the n -th load step assuming equilibrium solutions have been obtained for the previous load steps. The tangent stiffness is approximated by

$$K_{l-l'}^{(n)} \approx \left. \frac{\partial f_l^{\text{int}}}{\partial u_{l'}} \right|_{u=u^{(n-1)}} \quad (83)$$

The incremental form of the multiscale boundary condition is then expressed as

$$\Delta u_1^{(n)} = \Theta \Delta u_0^{(n)} + \Xi \Delta u_N^{(n)} \quad (84)$$

in which the bridging scale boundary condition operators are obtained in a similar way as described in the previous sections while assuming the periodicity of the tangent stiffness. By implementing the bridging-scale interface boundary condition, the multiscale simulation approach facilitates use of atomistic simulations for fine scale only, without involving the continuum modeling for the coarse scale, thereby providing elaborate atomistic information only when and where it is necessary. The robustness of this method is shown after comparison and verification of our results with benchmark results using full-sale molecular mechanics simulations.

5. Results and Discussion

In this section we implement benchmark problems to verify the proposed multiscale analysis method. We have used (10, 10) armchaired carbon nanotube consisting of 1900 atoms for all the results documented in sections 5.1 to 5.4. The nanotube has a length of 115.59 Å and a diameter of 13.56 Å before relaxation. The implementation can be further extended to nanotubes of other lengths and chiralities with requisite changes in the geometry of the unit cell. Another case of (40, 40) carbon nanotube is shown in section 5.5 to illustrate the computational efficiency. All the problems are treated as quasi-static, meaning the nanotube attains equilibrium (minimum energy configuration) after every incremental load step is imposed. The energy minimum in the fine scale region is obtained using the limited-memory BFGS method for large scale optimization [47]. We apply symmetric displacement boundary conditions to the unit cells at both the ends of the nanotube. The behavior of the nanotube is investigated under application of tensile, twisting and bending boundary conditions. In addition, we studied the tensile response of a tube with defects. We compare our results with those obtained after implementing full scale molecular mechanics simulations, hitherto considered as “analytical solutions”, on the same nanostructure under application of identical boundary conditions.

5.1 Tension and compression

In the tensile loading case, the nanotube is divided into two regions: the central fine scale region consisting of 1020 atoms and the coarse scale region consisting of the remaining 880 atoms. Incremental displacements of 0.24 Å per step are applied in the axial direction of the tube, while keeping the circular cross-section area of the tube intact. Displacements are applied only to the terminal unit cells at both ends of the tube. Figure 8 shows the change in potential energy (ΔU) vs. tensile strain ϵ in the CNT. The change in potential energy is measured with reference to the equilibrium potential energy of the unconstrained relaxed nanotube.

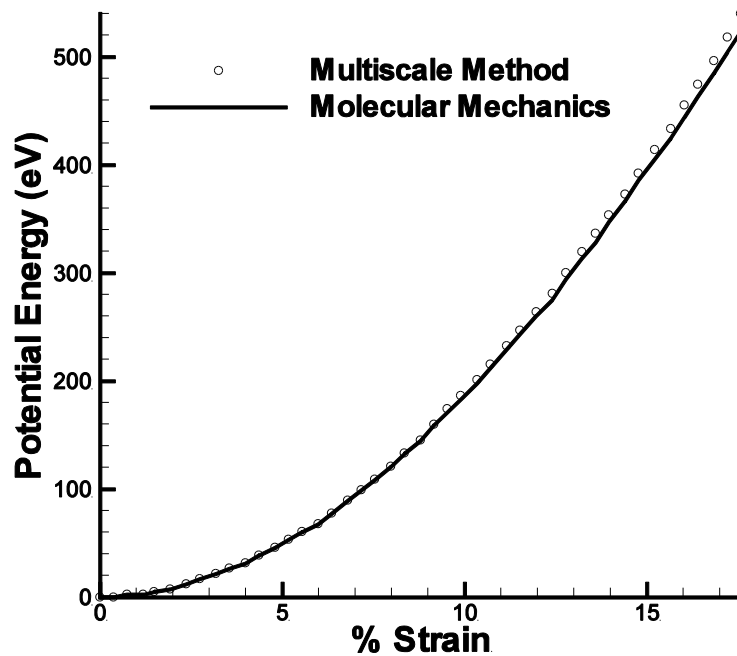


Figure 8. Comparison of variation of energy between molecular mechanics method and multiscale method under tensile loading conditions.

It can be observed that the results from the proposed multiscale method match closely with the benchmark full molecular mechanics results up to a strain of 17%. It can be realized that after a certain amount of deformation, the unit cells in the coarse scale region begin to lose their periodic nature. Since this contradicts the basic assumption of the method, for large strains the results obtained using the multiscale method start to deviate slightly from those obtained using the full atomistic simulations.

5.2 Twisting

The nanotube is divided into two regions, the fine scale region consisting of 1340 atoms at the center of the nanotube and the coarse scale region consisting of rest of 560 atoms. Twisting angles are imposed incrementally at the two ends of the nanotube while holding the cross-sectional circular shape unchanged. Loading steps of 0.5° are imposed till a total twisting angle

of 40° is reached. Figure 9(a) shows the twisted configuration of the nanotube while Figure 9(b) shows the graph of comparison of change in potential energy (ΔU) vs. the angle of twist in the CNT using the two methods.

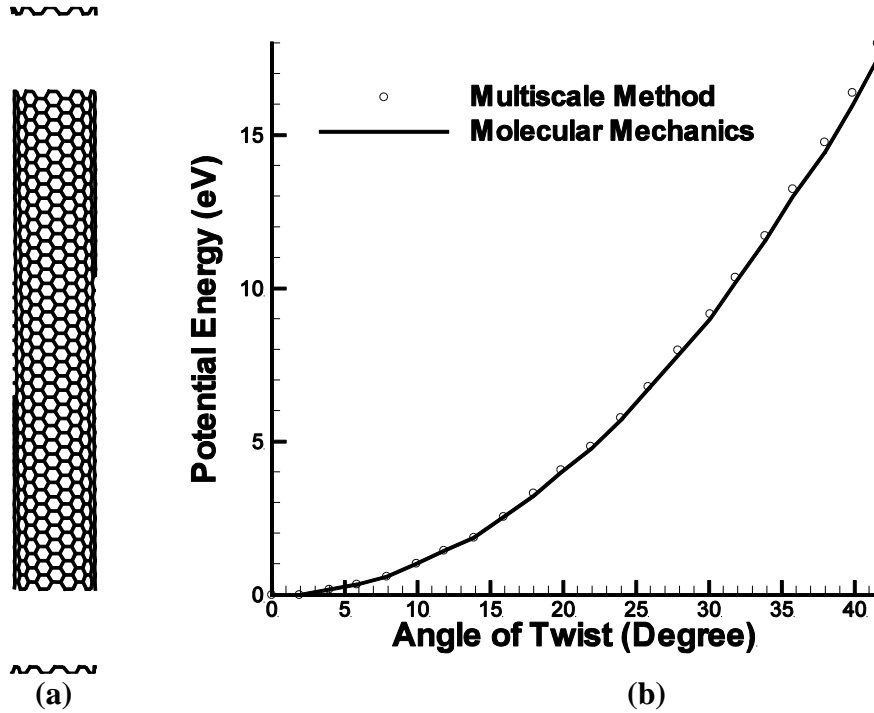


Figure 9. (a) Twisted pattern from multiscale method and (b) Energy comparison with molecular mechanics for the twisting loading case.

Similar conclusions can be drawn by observing from Figure 9 that the results from the multiscale method match closely with the benchmark full atomistic solution. As the twist in the nanotube goes on increasing, the nanotube slowly begins to lose its periodic nature along its axial direction. Hence for higher angular strains the results obtained using the multiscale method start to deviate from those obtained using molecular mechanics approach.

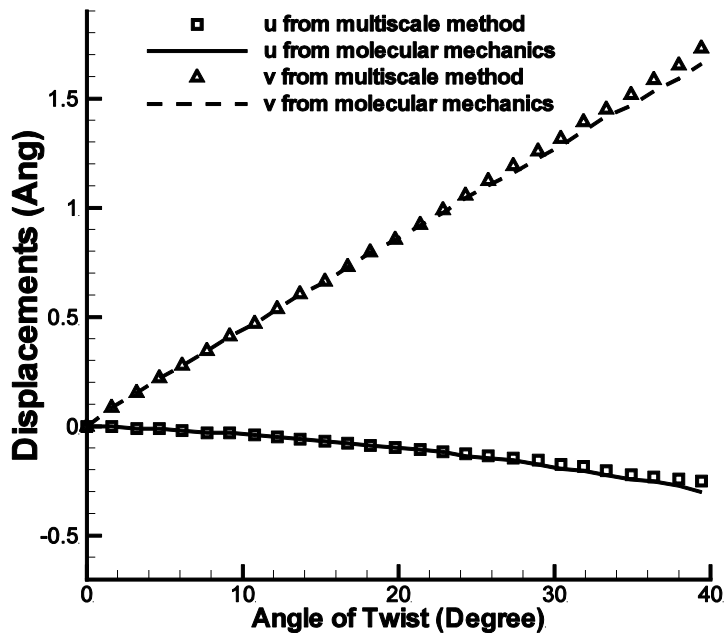


Figure 10. Comparison of atomic displacements in the interfacial cell using the molecular mechanics and multiscale technique.

Figure 10 shows the comparison of the x and y components of displacements (referred to as u and v , respectively) of an arbitrary atom in the interface unit cell during the loading process using the full scale molecular mechanics and the multiscale method. As can be seen, the proposed BC treatment predicts the displacements at the virtual interface fairly well up to moderately high deformation range.

The phenomenon of collapse or flattening of the tube is observed in the central region of the nanotube at a twisting angle of about 56° using full-scale atomistic simulation. Such a collapsed configuration has also been observed in experiment [48]. Our multiscale model is incapable of simulating this collapse since, even at inception, the collapsed region occupies a length greater than the total length of our fine scale region. The stiffness of the tube loses linearity at loads corresponding to collapse. Such a discrepancy is mainly due to the non-

localized nature of the collapse, which contradicts the assumption underlying our multiscale method.

5.3 Bending

In the case of bending, incremental bending angles of 0.375° are imposed on the terminating unit cells till a total bending angle of 45° is reached. Molecular mechanics solution is required only for the fine scale region consisting of 1020 atoms out of the 1900 atoms.

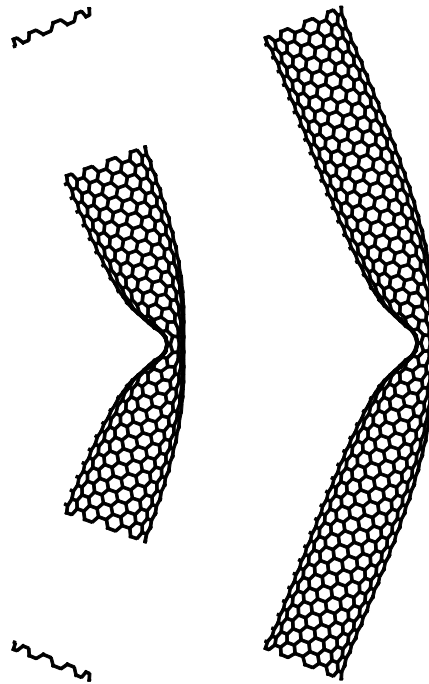


Figure 11. Comparison of the Post-buckling pattern of CNT from (left) Multiscale method (Right) Molecular mechanics.

As has been shown using full atomistic simulation, the nanotube buckles at a bending angle of about 12° . Buckling due to bending and torsion has been earlier demonstrated in [49-50], and is characterized by a collapse in the cross-section which results in a kink or ribbon-like structure. Experimental observations of buckling in CNT have been documented in [51-53]. A major factor that contributes to the buckling mode is the radial deformability of the tubes. Figure 12 shows the post-buckling patterns as obtained from the multiscale simulations and full-scale molecular mechanics approach. As can be seen from this comparison, the new multiscale method

not only captures the pre-buckling behavior of the tube but also simulates the post collapse behavior accurately. This can be due to the local nature of the buckling phenomenon that is confined to the fine scale region alone.

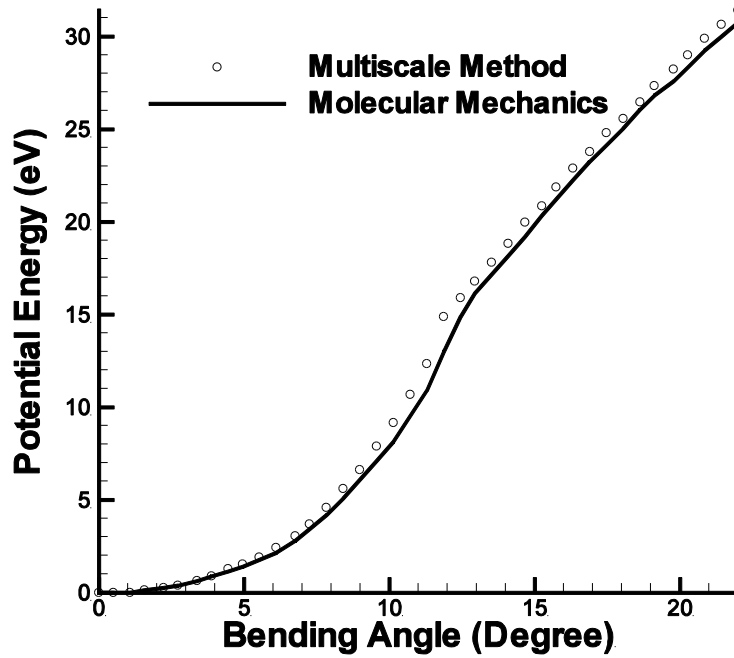


Figure 12. Bending results: comparison of variation of bending energy between molecular mechanics method and multiscale method.

Figure 12 shows the graph of change in potential energy (ΔU) vs. the bending angle of the CNT. It can be observed that the result obtained using the multiscale method starts to deviate as the bending angle increases to about 12° . This can be attributed to the commencement of the loss of periodicity of the unit cells of the nanotube due to non-linear deformation pattern of the tube in the pre-buckling zone. After the tube buckles, the energy variation assumes a near linear shape so that the energy variation obtained using the full atomistic simulation matches closely with that obtained using the multiscale method. This indicates that the local deformation in the nanotube can be well captured using the multiscale method. The advantage of the multiscale

simulation can be easily seen from the fact that detailed atomistic deformations in the nanotube are captured with the help of atomistic simulations in the fine scale region. Figure 13 shows the stepwise progress of the nanotube bending resolved using the multiscale approach.

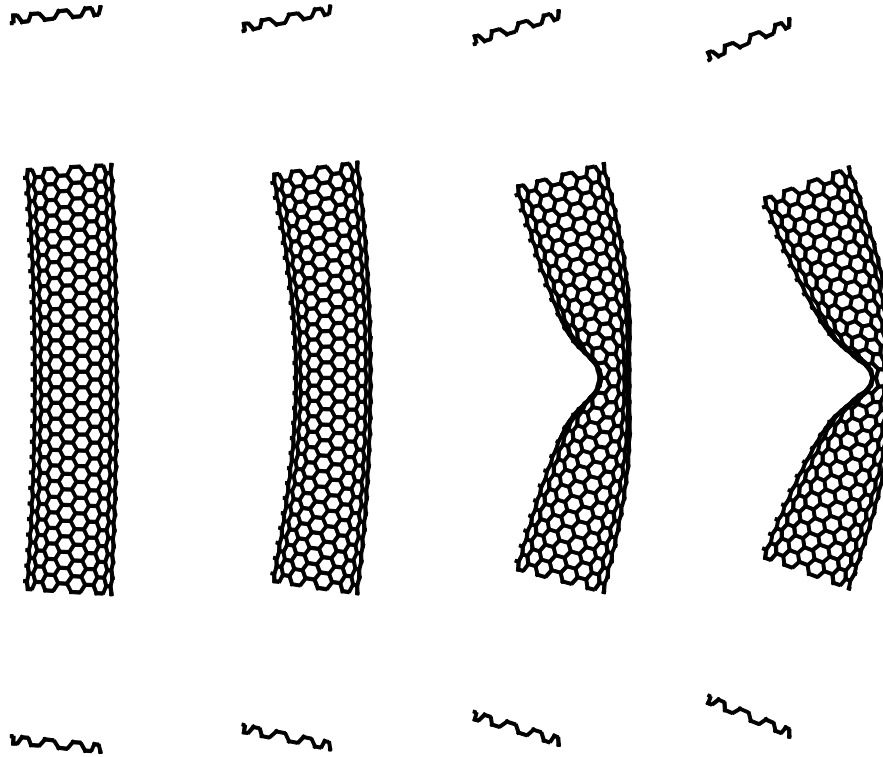


Figure 13. Progress of bending of CNT as seen using multiscale simulation.

5.4 Loading of nanotubes with defects

One of the common defects observed in carbon nanotubes is the absence of chemical bonds between adjacent carbon atoms at random locations. We simulate the behavior of CNTs with broken bonds to capture their behavior under realistic conditions. Three parallel bonds making an angle of 30° with the nanotube axis in the fine scale region are considered absent and the behavior of the tube is observed under tensile loading conditions.

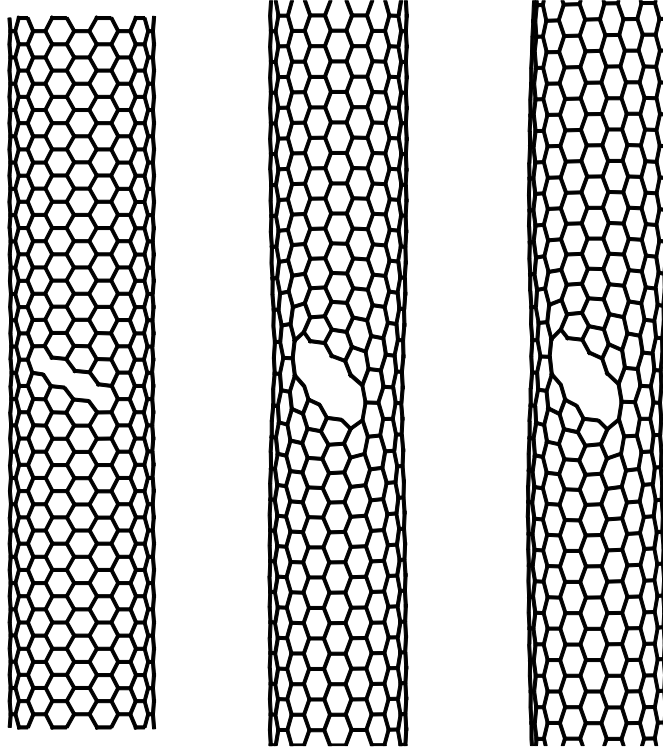


Figure 14. Nanotube with broken bonds (a) The original configuration of CNT with vacancies as defects. (b) The CNT under tension at 12% strain and (c) 16% strain using the proposed bridging-scale boundary condition.

The nanotube is divided into two regions, the central fine scale region consisting of 1020 atoms and the coarse scale region consisting of the remaining 880 atoms. Incremental displacements of 0.24 \AA per step are imposed on the unit cells at the two ends of the tube, only in the axial direction, while keeping the circular cross-section area of the tube intact. As shown in Figure 14, the simulation of behavior of the nanotube using the newly proposed method matches well with that obtained using full atomistic method for moderately high strains. Figure 15 shows the graph of change in potential energy (ΔU) vs. percentage strain ϵ in the CNT. It can be observed that the results from the multiscale method match closely with the benchmark molecular mechanics results.

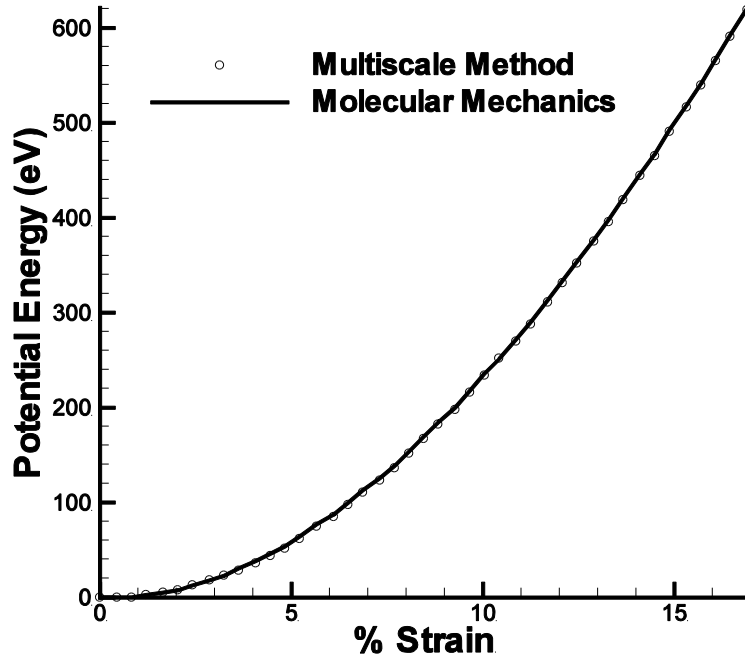


Figure 15. Comparison of variation of energy between molecular mechanics method and multiscale method under tensile loading conditions.

5.5 3D Buckling in a (40,40) tube

In all the benchmark problems shown above, the size of the fine scale region is comparable to that of the coarse scale. In order to demonstrate the computational efficiency of the method, we proceed to simulate the bending of a 125 nm long (40,40) CNT with 81,280 atoms. This corresponds to 508 unit cells in the axial direction. Both ends of the tube are subjected to bending angle of 0.01° per step and a total bending of 10° is imposed. In the multiscale implementation, only the 11,200 atoms in the central region are subjected to molecular mechanics simulation, with the boundary condition derived from the proposed method. Shown in Figure 16 is a set of snapshot of the fine scale region where the buckling develops at bending angles of 2.5° , 5.0° , 7.5° and 10° . The rings on the top and bottom illustrate the regions where the far-field bending boundary condition is imposed. The color

intensity in the fine scale region indicates the potential energy of each atom, which shows that the energy values in localized region are much more intensive. Unlike the (10,10) case, the buckling pattern in this case is more complex. Four distinctive buckled regions are shown and their common edge shows an “X” pattern. Similar results have also been reported earlier in the case of multi-walled tubes. To verify the method, full-scale atomistic simulation based on molecular mechanics approach is carried out on the same computing platform (Intel Xeon E5502 processor with 4GB memory and Redhat Linux operating system). The full-scale simulation takes ~35 hrs to complete, while the running time for the multiscale method is close to 2 hrs. The speed up of the method is thus clearly demonstrated. To examine the accuracy of the method, the bending energy values are compared and shown in Figure 17. Good agreement can be observed before the buckling occurs. In terms of predicting the onset of the buckling, the prediction from the multiscale method differs from the full scale simulation by 0.24 degree of bending angle. Such a difference is mainly due to the periodicity assumption we have made as an approximation. In the post-buckling stage, we again observe good agreement between the two methods.

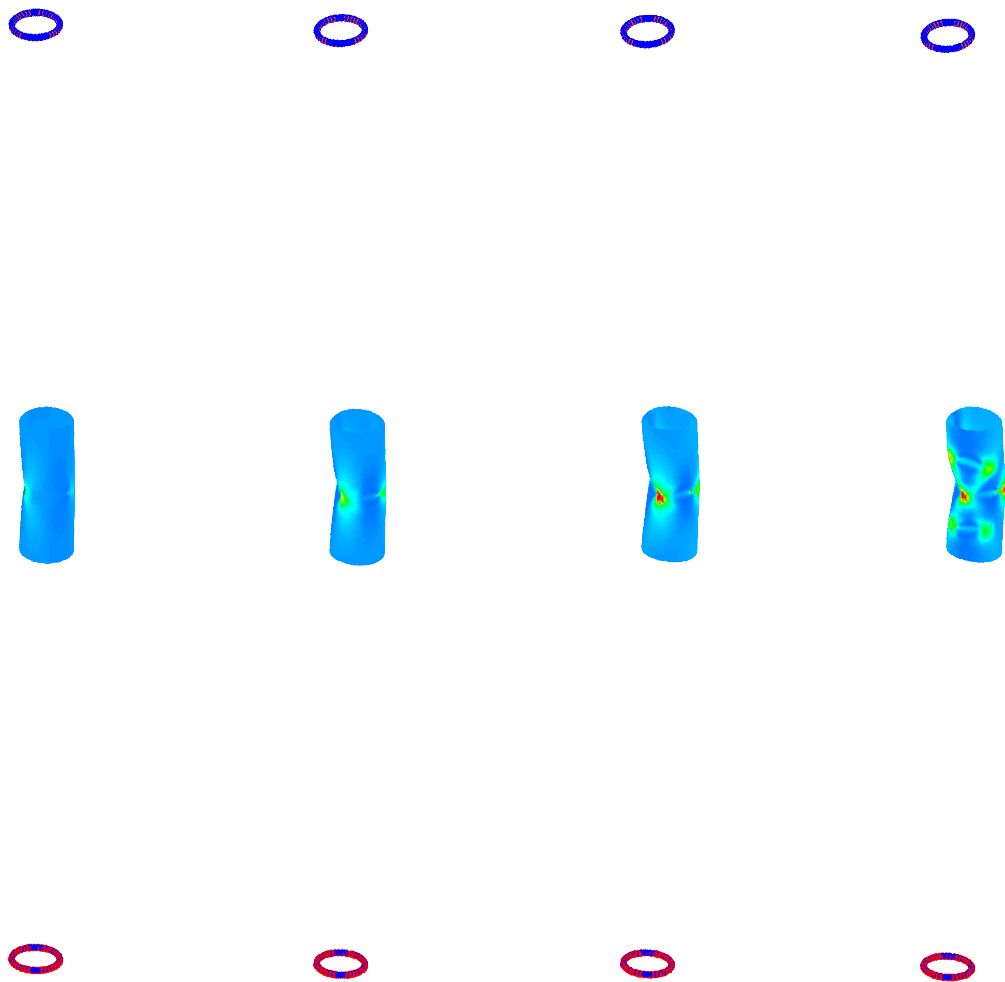


Figure 16 Development of buckling in a (40,40) tube subjected to bending.

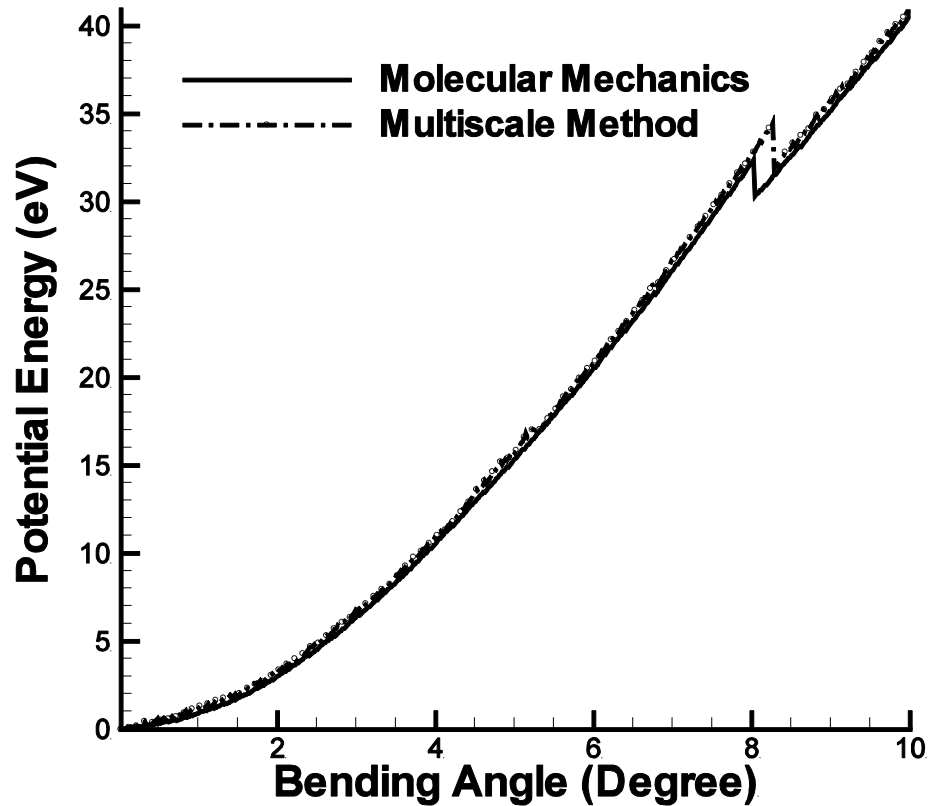


Figure 17 Comparison of the bending energy between the two methods for the (40,40) CNT.

6. Conclusions

Multiscale modeling and simulation techniques are important tools for developing a comprehensive understanding of mechanics of nanoscale materials. In this paper, we have discussed an analytical approach to formulate the multiscale boundary conditions for quasistatic atomistic simulations of periodic atomic structures. Under the premise of translational symmetry of the coarse grain lattice, we have used Discrete Fourier Transform and the Green's functions to yield a compact formulation in terms of the discrete convolution operators, which relate the applied boundary conditions to a set of equivalent virtual boundary conditions. These virtual boundary conditions applied on a reduced domain produce the same effect in the region of

interest as that of the actual boundary conditions. Thus our domain of analysis is confined to a smaller size, while adequately preserving the accuracy.

It is important to note that our approach applies the continuum concepts at the atomic scale to eliminate the computation of unnecessary degrees of freedom of the coarse scale region. It does not require coarse scale elements to be scaled down to the atomic level at the virtual boundary between fine and coarse scales as being done by many other approaches. Thus our method obviates the necessity of building the actual coarse scale model by exploiting its structural periodicity.

We have implemented a series of benchmark problems involving realistic boundary conditions on carbon nanotubes. We have found that the method yields results in accordance with existing full scale atomistic simulations, thus ensuring its robustness and reliability. The energy comparison show that the overall behavior of the atoms in the fine scale region matches closely to that predicted by full scale atomistic simulations. As a general observation, the results predicted by the multiscale method are slightly on the conservative side as compared to the full scale atomistic simulations. As demonstrated in the last example problem, the method is well suited for problems that are governed by local mechanics since there is no need to simulate the whole region. As such, the proposed approach achieves significant computational saving.

While the applications presented in this paper are relatively simple, we believe the methodology can be extended to other nanocrystalline structures in a straightforward manner. Since most of these nanocrystalline structures have well-defined unit cells, the bridging-scale interface boundary condition will be tied to the specific material system. The major implementation involves includes utilizing the corresponding inter-atomic potential and deriving the kernel matrix. The proposed methodology can also be incorporated into a concurrent

simulation scheme in which both the coarse and fine scale phenomena involved may be of interest.

7. Acknowledgement

Dong Qian and Eduard Karpov would like to acknowledge the general support from the National Science Foundation (grants CMMI 0600583, 0700107 and 0900498). Wing Kam Liu is supported by NSF grant CMMI 0823327. Any opinions, findings, conclusions, or recommendations expressed in these documents are those of the author(s) and do not necessarily reflect the views of the National Science Foundation.

Appendix A

The proof of Eq.(60) as given in [37, 38] is briefly discussed here. Let be x_k be the roots of the Eq. $x^n + 1 = 0$ such that n is a positive integer and $k=1, 2, 3, \dots, n$. Then for a positive integer m , [43] states, by the method of partial fractions,

$$\frac{x^m}{x^n + 1} = -\frac{1}{n} \sum_{k=1}^n \frac{x_k^{m+1}}{(x - x_k)}, \quad 0 \leq m < n \quad (1)$$

An addition of unity to the right hand side makes the Eq.(1) true for $m = n$.

Differentiating Eq.(1) and then setting $x = 1$, we have

$$\frac{(2m - n)n}{4} = \sum_{k=1}^n \frac{x_k^{m+1}}{(1 - x_k)^2}, \quad 0 \leq m \leq n \quad (2)$$

The roots x_k can be expressed as $x_k = e^{(2k-1)\pi i/n}$, hence,

$$x_k^m + x_k^{-m} = 2 \cos(m(2k - 1)\pi/n) \quad (3)$$

$$x_k^m - x_k^{-m} = 2i \sin(m(2k - 1)\pi/n) \quad (4)$$

The denominator of Eq.(2) can be transformed as:

$$\begin{aligned} (1 - x_k)^2 &= -x_k(1 - x_k^{-1})(1 - x_k) = -x_k[2 - (x_k + x_k^{-1})] \\ &= -2x_k[1 - \cos((2k - 1)\pi/n)] \end{aligned} \quad (5)$$

Substituting Eq.(5) in Eq.(2), we get,

$$\sum_{k=1}^n \frac{x_k^m}{[1 - \cos((2k - 1)\pi/n)]} = \frac{(n - 2m)n}{2} \quad (6)$$

Since the roots x_k are complex conjugate pairs, $x_k^{-1} = e^{-(2k-1)\pi i/n}$ are also roots of the equation. Thus we have,

$$\sum_{k=1}^n \frac{x_k^{-m}}{[1 - \cos((2k-1)\pi/n)]} = \frac{(n-2m)n}{2} \quad (7)$$

Adding equations (6) and (7) and using Eq.(3) we get,

$$\sum_{k=1}^n \frac{\cos(m(2k-1)\pi/n)}{1 - \cos((2k-1)\pi/n)} = \frac{(n-2m)n}{2}, \quad 0 \leq m \leq n \quad (8)$$

i.e.,

$$\sum_{k=1}^n \frac{\cos(m(2k-1)\pi/n)}{\sin^2((2k-1)\pi/2n)} = (n-2m)n \quad (9)$$

Combining the terms for k and $n-k+1$, we arrive at,

$$\sum_{k=1}^{n/2} \frac{\cos(m(2k-1)\pi/n)}{\sin^2((2k-1)\pi/2n)} = (n-2m)\frac{n}{2} + \left\{ \left[\frac{n}{2} \right] - \frac{n}{2} \right\} (-1)^m \quad (10)$$

which is the same as Eq.(60) in the main text.

1. Tadmor, E.B., M. Ortiz, and R. Phillips, Quasicontinuum analysis of defects in solids. *Philosophical Magazine A-Physics Of Condensed Matter Structure Defects And Mechanical Properties*, 1996. **73**(6): p. 1529-1563.
2. Tadmor, E.B., R. Phillips, and M. Ortiz, Mixed atomistic and continuum models of deformation in solids. *Langmuir*, 1996. **12**(19): p. 4529-4534.
3. Rodney, D. and R. Phillips, Structure and strength of dislocation junctions: An atomic level analysis. *Physical Review Letters*, 1999. **82**(8): p. 1704-1707.
4. Shin, C.S., M.C. Fivel, D. Rodney, R. Phillips, V.B. Shenoy, and L. Dupuy, Formation and strength of dislocation junctions in FCC metals: A study by dislocation dynamics and atomistic simulations. *Journal De Physique Iv*, 2001. **11**(PR5): p. 19-26.
5. Shenoy, V.B., R. Miller, E.B. Tadmor, R. Phillips, and M. Ortiz, Quasicontinuum models of interfacial structure and deformation. *Physical Review Letters*, 1998. **80**(4): p. 742-745.
6. Shenoy, V.B., R. Miller, E.B. Tadmor, D. Rodney, R. Phillips, and M. Ortiz, An adaptive finite element approach to atomic-scale mechanics - the quasicontinuum method. *Journal Of The Mechanics And Physics Of Solids*, 1999. **47**(3): p. 611-642.
7. Tadmor, E.B., R. Miller, R. Phillips, and M. Ortiz, Nanoindentation and incipient plasticity. *Journal Of Materials Research*, 1999. **14**(6): p. 2233-2250.
8. Miller, R., E.B. Tadmor, R. Phillips, and M. Ortiz, Quasicontinuum simulation of fracture at the atomic scale. *Modelling And Simulation In Materials Science And Engineering*, 1998. **6**(5): p. 607-638.
9. Qian, D., G.J. Wagner, and W.K. Liu, A multiscale projection method for the analysis of carbon nanotubes. *Computer Methods In Applied Mechanics And Engineering*, 2004. **193**(17-20): p. 1603-1632.
10. Adelman, S.A. and J.D. Doll, Generalized Langevin equation approach for atom/solid-surface scattering-collinear atom/harmonic chain model. *J. Chem. Phys.*, 1974. **61**(10): p. 4242-4245.
11. Adelman, S.A. and J.D. Doll, Generalized Langevin equation approach for atom/solid surface scattering - general formulation for classical scattering of harmonic solids. *J. Chem. Phys.*, 1976. **64**(6): p. 2375-2388.
12. Cai, W., M. de Koning, V.V. Bulatov, and S. Yip, Minimizing boundary reflections in coupled-domain simulations. *Physical Review Letters*, 2000. **85**(15): p. 3213-3216.
13. E, W. and Z.Y. Huang, Matching conditions in atomistic-continuum modeling of materials. *Physical Review Letters*, 2001. **87**13(13).
14. Wagner, G.J. and W.K. Liu, Coupling of atomistic and continuum simulations using a bridging scale decomposition. *Journal of Computational Physics*, 2003. **190**(1): p. 249-274.
15. Kadowaki, H. and W.K. Liu, Bridging multiscale method for localization problems. *Computer methods in applied mechanics and engineering*, 2004. **193**: p. 3267-3302.
16. Park, H.S., E.G. Karpov, P.A. Klein, and W.K. Liu, Three-dimensional bridging scale analysis of dynamic fracture. *Journal of Computational Physics*, 2005. **207**(2): p. 588-609.

17. Liu, W.K., H.S. Park, D. Qian, E.G. Karpov, H. Kadowaki, and G.J. Wagner, Bridging scale methods for nanomechanics and materials. *Computer Methods In Applied Mechanics And Engineering*, 2006. **195**(13-16): p. 1407-1421.
18. Tang, S.Q., W.K. Liu, E.G. Karpov, and T.Y. Hou, Bridging atomistic/continuum scales in solids with moving dislocations. *Chinese Physics Letters*, 2007. **24**(1): p. 161-164.
19. Farrell, D.E., E.G. Karpov, and W.K. Liu, Algorithms for bridging scale method parameters. *Computational Mechanics*, 2007. **40**(6): p. 965-978.
20. Farrell, D.E., H.S. Park, and W.K. Liu, Implementation aspects of the bridging scale method and application to intersonic crack propagation. *International Journal For Numerical Methods In Engineering*, 2007. **71**(5): p. 583-605.
21. Karpov, E.G., G.J. Wagner, and W.K. Liu, A Green's function approach to deriving non-reflecting boundary conditions in molecular dynamics simulations. *International Journal For Numerical Methods In Engineering*, 2005. **62**(9): p. 1250-1262.
22. Gonella, S. and M. Ruzzene, Bridging scales analysis of wave propagation in heterogeneous structures with imperfections. *Wave Motion*, 2008. **45**(4): p. 481-497.
23. Park, H.S., E.G. Karpov, W.K. Liu, and P.A. Klein, The bridging scale for two-dimensional atomistic/continuum coupling. *Philosophical Magazine*, 2005. **85**(1): p. 79-113.
24. Liu, W.K., S. Jun, and D. Qian, Computational nanomechanics of materials. *Journal Of Computational And Theoretical Nanoscience*, 2008. **5**(5): p. 970-996.
25. To, A.C., W.K. Liu, and A. Kopacz, A finite temperature continuum theory based on interatomic potential in crystalline solids. *Computational Mechanics*, 2008. **42**(4): p. 531-541.
26. Medyanik, S.N. and W.K. Liu, Multiple time scale method for atomistic simulations. *Computational Mechanics*, 2008. **42**(4): p. 569-577.
27. Karpov, E.G., H. Yu, H.S. Park, W.K. Liu, Q.J. Wang, and D. Qian, Multiscale boundary conditions in crystalline solids: Theory and application to nanoindentation. *International Journal Of Solids And Structures*, 2006. **43**(21): p. 6359-6379.
28. Karpov, E.G., S. Chaichenets, W.K. Liu, and D. Qian, Mechano-kinetic coupling approach for materials with dynamic internal structure. *Philosophical Magazine Letters*, 2010. **90**(7): p. 471-480.
29. Medyanik, S.N., E.G. Karpov, and W.K. Liu, Domain reduction method for atomistic simulations. *Journal of Computational Physics*, 2006. **218**(2): p. 836-859.
30. Xiao, S.P. and T. Belytschko, A bridging domain method for coupling continua with molecular dynamics. *Computer Methods in Applied Mechanics and Engineering*, 2004. **193**(17-20): p. 1645-1669.
31. Xu, M. and T. Belytschko, Conservation properties of the bridging domain method for coupled molecular/continuum dynamics. *International Journal For Numerical Methods In Engineering*, 2008. **76**(3): p. 278-294.
32. Li, S.F., X.H. Liu, A. Agrawal, and A.C. To, Perfectly matched multiscale simulations for discrete lattice systems: Extension to multiple dimensions. *Physical Review B*, 2006. **74**(4).
33. Chirputkar, S.U. and D. Qian, Coupled atomistic/continuum simulation based on extended space-time finite element method. *Cmes-Computer Modeling In Engineering & Sciences*, 2008. **24**(2-3): p. 185-202.

34. Qian, D., W.K. Liu, and Q.J. Zheng, Concurrent quantum/continuum coupling analysis of nanostructures. *Computer Methods In Applied Mechanics And Engineering*, 2008. **197**(41-42): p. 3291-3323.
35. Liu, W.K., D. Qian, S. Gonella, S.F. Li, W. Chen, and S. Chirptukar, Multiscale methods for mechanical science of complex materials: bridging from quantum to stochastic multiresolution continuum (to appear). *International Journal For Numerical Methods In Engineering*, 2010.
36. Liu, W.K., E.G. Karpov, and H.S. Park, *Nano mechanics and materials: theory, multiscale methods and applications*. 2006: John Wiley & Sons, Ltd.
37. Ryvkin, M., M.B. Fuchs, and B. Nuller, Optimal design of infinite repetitive structures. *Structural Optimization*, 1999. **18**(2-3): p. 202-209.
38. Moses, E., M. Ryvkin, and M.B. Fuchs, A FE methodology for the static analysis of infinite periodic structures under general loading. *Computational Mechanics*, 2001. **27**(5): p. 369-377.
39. Karpov, E.G., N.G. Stephen, and D.L. Dorofeev, On static analysis of finite repetitive structures by discrete Fourier transform. *International Journal Of Solids And Structures*, 2002. **39**(16): p. 4291-4310.
40. Karpov, E.G., *Periodic lattice structures: Discrete Functional Solutions and Probabilistic Methods of Statics*. 2009: Lambert Academic Publishing.
41. Brenner, D.W., Empirical Potential for Hydrocarbons for Use in Simulating the Chemical Vapor-Deposition of Diamond Films. *Physical Review B*, 1990. **42**(15): p. 9458-9471.
42. **Hansen, E.R., A table of series and products**. 1975, Englewood Cliffs, N. J.: Prentice-Hall.
43. Dunkel, O., *American Mathematical Monthly*, 1938. **45**(4): p. 255-257.
44. Qian, D., G.J. Wagner, W.K. Liu, M.F. Yu, and R.S. Ruoff, Mechanics of carbon nanotubes. *Applied Mechanics Reviews*, 2002. **55**(6): p. 495-533.
45. Abell, G.C., Empirical Chemical Pseudopotential Theory Of Molecular And Metallic Bonding. *Physical Review B*, 1985. **31**(10): p. 6184-6196.
46. Nocedal, J., Updating Quasi-Newton Matrices with Limited Storage. *Mathematics of Computation*, 1980. **35**(151): p. 773-782.
47. Zhu, C.Y., R.H. Byrd, P.H. Lu, and J. Nocedal, Algorithm 778: L-BFGS-B: Fortran subroutines for large-scale bound-constrained optimization. *Acm Transactions On Mathematical Software*, 1997. **23**(4): p. 550-560.
48. Yu, M.F., M.J. Dyer, J. Chen, D. Qian, W.K. Liu, and R.S. Ruoff, Locked twist in multi-walled carbon nanotube ribbons. *Physical Review B, Rapid Communications*, 2001. **64**: p. 241403R.
49. Yakobson, B.I., C.J. Brabec, and J. Bernholc, Nanomechanics of carbon tubes: Instabilities beyond linear response. *Physical Review Letters*, 1996. **76**(14): p. 2511-2514.
50. Qian, D., W.K. Liu, S. Subramoney, and R.S. Ruoff, Effect of interlayer potential on mechanical deformation of multiwalled carbon nanotubes. *Journal Of Nanoscience And Nanotechnology*, 2003. **3**(1-2): p. 185-191.
51. Falvo, M.R., G.J. Clary, R.M. Taylor, V. Chi, F.P. Brooks, S. Washburn, and R. Superfine, Bending and buckling of carbon nanotubes under large strain. *Nature*, 1997. **389**(6651): p. 582-584.

52. Lourie, O., D.M. Cox, and H.D. Wagner, Buckling and collapse of embedded carbon nanotubes. *Physical Review Letters*, 1998. **81**(8): p. 1638-1641.
53. Wong, E.W., P.E. Sheehan, and C.M. Lieber, Nanobeam mechanics: Elasticity, strength, and toughness of nanorods and nanotubes. *Science*, 1997. **277**(5334): p. 1971-1975.